

AutoBCS: Block-based Image Compressive Sensing with Data-driven Acquisition and Non-iterative Reconstruction

Hongping Gan, Yang Gao, Chunyi Liu, Haiwei Chen, and Feng Liu

arXiv:2009.14706v1 [eess.SP] 30 Sep 2020

Abstract—Block compressive sensing is a well-known signal acquisition and reconstruction paradigm with widespread application prospect of science, engineering and cybernetic systems. However, the state-of-the-art block-based image compressive sensing (BCS) generally suffer from two issues. The sparsifying domain and the sensing matrices widely used for image acquisition are not data-driven, thus ignoring both the features of the image and the relationship among sub-block images. Moreover, it requires to address high-dimensional optimization problem with extensive computational complexity for image reconstruction. In this paper, we provide a deep learning strategy for BCS, called AutoBCS, which takes into account the prior knowledge of image in the acquisition step and establishes a subsequent reconstruction model to obtain fast image reconstruction with low computational cost. More precisely, we present a learning-based sensing matrix (LSM) from training data so as to accomplish image acquisition, therefore capturing and preserving more image characteristics. In particular, the generated LSM is proved to satisfy the theoretical requirements, such as the so-called restricted isometry property. Additionally, we build a non-iterative reconstruction network, which provides an end-to-end BCS reconstruction to eliminate blocking artifacts and maximize image reconstruction accuracy, in our AutoBCS architecture. Furthermore, we investigate comprehensive comparison studies with both traditional BCS approaches as well as newly-developing deep learning methods. Compared with these approaches, our AutoBCS framework can not only provide superior performance in both image quality metrics (SSIM and PSNR) and visual perception, but also automatically benefit reconstruction speed.

Index Terms—Deep Learning, Image Compressive Sensing, Block Diagonal Matrix, Data-driven Acquisition, Fast Image Reconstruction

I. INTRODUCTION

Compressive sensing(CS) has renewed explosive interest in essential sampling techniques with the goal being to acquire and reconstruct signals at sub-Nyquist sampling rates. It automatically enables *data hardware compression* during the sampling process of the signals of interest $\mathbf{x} \in \mathbb{R}^n$, which provides significantly potential of lifting the energy efficiency of sensors in modern signal processing applications. Under the guidance of a series of landmark works of Candès [1] and

Donoho [2], there have emerged a large number of CS-based applications in recent years, such as single-pixel camera [3], data security [4, 5], multilayer network [6], and transcriptomic profiling [7].

Mathematically, CS states that \mathbf{x} can be exactly reconstructed from a set of non-adaptive measurements formed by $\mathbf{y} = \mathbf{B} \cdot \mathbf{x}$ with \mathbf{B} of size $m \times n$ ($m \ll n$), assuming that \mathbf{x} has sparsity property and the sensing matrix (sampling patterns) \mathbf{B} meets certain structural conditions. Note that the number of measurements, m , is on the order of the information-theoretic dimension instead of that of linear-algebraic ambient dimension of \mathbf{x} [8]. Obviously, the sparsity property of \mathbf{x} , sensing matrix \mathbf{B} , and nonlinear reconstruction are three ingredients for perfect reconstruction in CS theory.

Sparsity property. Signals of interest can always be well-represented as a linear combination with just a few entries from a certain dictionary or basis. Let's focus on the sparse signal firstly. A signal \mathbf{x} is regarded as s -sparse when $\|\mathbf{x}\|_0 \leq s$. Let

$$\Sigma_s = \{\mathbf{x} : \|\mathbf{x}\|_0 \leq s\}. \quad (1)$$

be the array of all s -sparse signals. In general, we always deal with that \mathbf{x} is not itself sparse, but it admits a well-approximated sparse in a sparsifying basis $\Psi \in \mathbb{R}^n$. If so, we can write \mathbf{x} as $\mathbf{x} = \Psi \cdot \mathbf{v}$ with \mathbf{v} being s -sparse. Originally, typical choices of transform basis for image sparse regularization include discrete cosine transform [9], wavelet domain [10], and etc.. However, these conventional sparse regularizations cannot seize higher-order dependency of coefficient vector \mathbf{v} . To capture their dependence, various specialized and sophisticated regularizations have been exploited for CS of images, most remarkably, group/structured sparsity [11, 12], Bayesian/model-based sparsity [13], low-rank regularization [14], and non-local sparsity [15]. These sparse regularizations can develop interpretable sparsity prior of \mathbf{x} , resulting in that the corresponding reconstruction approaches often provide more accurate and efficient reconstruction. For optimal CS recovery, unfortunately, the aforementioned sparsity regularizations are either not data-driven learned or predefined in CS-based image applications.

Sensing matrix. The sensing matrix \mathbf{B} should satisfy certain structural properties in order to seize and preserve the salient information of \mathbf{x} during linear dimensionality reduction: $\mathbb{R}^n \rightarrow \mathbb{R}^m$. An elegant property of \mathbf{B} that guarantees such signal acquisition is called restricted isometry property (RIP) [16] if

This work was supported in part by National Natural Science Foundation of China under Grant 61372069, in part by the Chongqing Municipal Education Commission under Grant KJ1501105, and in part by the 111 Project of China under Grant B08038.

Hongping Gan is with the School of Software, Northwestern Polytechnical University, Xi'an 710072, China (e-mail: hongpinggan@nwpu.edu.cn)

Yang Gao, Chunyi Liu, Haiwei Chen and Feng Liu are with the School of Information Technology and Electrical Engineering, The University of Queensland, Brisbane, QLD 4072, Australia (e-mail: {yang.gao; chunyi.liu; haiwei.chen; feng}@uq.edu.au)

\mathbf{B} approaches Σ_s as an approximate isometry. More formally, a matrix \mathbf{B} satisfies the (s, δ_s) -RIP if

$$\forall \mathbf{x} \in \Sigma_s, \quad (1 - \delta) \leq \frac{\|\mathbf{B}\mathbf{x}\|_2^2}{\|\mathbf{x}\|_2^2} \leq (1 + \delta), \quad (2)$$

where the smallest constant $\delta_s \leq \delta$ obeying Eq. (2) is referred to as the restricted isometry constant. Other famous properties for selecting \mathbf{B} include the coherence [17], the spark [8], and the null space property [18]. Based on these guide properties, numerous insightful sensing matrices have by now been introduced for CS applications [19–21]. In particular, it is widely believed that random matrices (e.g. Gaussian sensing matrix) can allow us to perfectly reconstruct \mathbf{x} from only $\mathcal{O}(\log(n/s))$ measurements in polynomial time through different reconstruction algorithms [22]. However, the sensing matrices used in practical CS applications are often signal independent, which discards some prior information of signal.

Nonlinear reconstruction. With the obtained measurements \mathbf{y} and the transform sparsity of \mathbf{x} , it is a well-established fact that we can reconstruct the original signal \mathbf{x} via the following optimization problem:

$$\tilde{\mathbf{x}} = \arg \min_{\mathbf{x}} \frac{1}{2} \|\mathbf{B}\mathbf{x} - \mathbf{y}\|_2^2 + \lambda \|\Psi\mathbf{x}\|_1, \quad (3)$$

where λ denotes the regularization parameter. We can refer to this procedure as a nonlinear reconstruction mapping $\tilde{\mathbf{x}} = f(\mathbf{y})$. An intuitive way to solve Eq. (3) is to utilize a convex programming method. However, such a method often suffers from high computational complexity when handling large signals, such as image. To avoid this, a variety of lower cost iterative approaches have been developed, including iterative shrinkage-thresholding algorithm (ISTA) [23], alternating direction method of multipliers (ADMM) [24], and approximate message passing [25], to name just a few. Although these algorithms benefit convergence guarantee and theoretical analysis, the involved parameters (e.g., penalty parameters and step size) are always hand-crafted in the solvers. Moreover, they usually need hundreds of iterations to converge to a (sub-)optimal solution, leading to that the whole process is much time consuming and may take a few minutes.

In summary, the aforementioned three issues are the core issues of CS. From a theoretical perspective, the general-purpose CS is always effective. However, practitioners in most engineering applications are often faced with the industrial bottlenecks, such as big data problem, high memory requirement, slow reconstruction speed. Many efficient strategies have been exploited to promote CS from theory to industry, including block CS [26], infinite dimensional CS [27], and quantized CS [28], etc..

A. Motivation

Over the past decade, block CS has drawn particular interest as it shows widespread application prospect of science and engineering such as sparse subspace clustering [29], spectrum sensing [30], as well as multiple measurement vector [31]. In particular, such a block-based CS framework has been successfully adapted to image acquisition systems so as to

relieve the burdens in both memory and energy consumption of sensor, and reconstruction algorithms [26]. As a consequence, the block-based image compressive sensing (BCS) is extraordinarily desirable for low-power imaging devices (e.g., wireless visual sensor network) because of their limited computation capabilities. Compared with the traditional general-purpose CS of image, BCS usually benefits the following aspects. Firstly, block-based measurement is naturally suitable for real-time, energy-limited imaging applications since it avoids dealing with high-dimensional data. Secondly, we can accelerate the image reconstruction as each sub-block image is independently handled. Thirdly, the sensing operator only takes a small amount of memory and corresponds to feasible hardware architectures owing to its structured construction.

The initial BCS framework introduced by Gan et.al [26] contains two separate phases: sampling and reconstruction. In the sampling phase, the original signal/image of interest is divided into non-overlapping sub-block images, then each sub-block is independently measured via the same sensing operator. In other words, the so-called BCS accomplishes image acquisition in a block-by-block style. We can consider the equivalent full sensing matrix in BCS as a block diagonal matrix whose sub-blocks are identical copies of the used sensing operator. In the reconstruction phase, linear estimation coupled with two-stage iterative hard thresholding has been devoted to reconstruct the original image. Following this baseline framework, some sophisticated reconstruction algorithms have been proposed to further improve the performance of BCS by exploiting either extra optimization criteria [32, 33] or image priors [34, 35], such as smoothed projected Landweber reconstruction (SPL) [32, 36], collaborative sparsity (RCoS) [34], and group-based sparse representation (GbSR) [35].

Although the aforementioned algorithms have promising performance and are beneficial with theoretical analysis, they are still encountered the challenges of adjusting parameters because they are essentially iterative algorithms solving Eq. (3). Moreover, the transform domain and sensing operator in the BCS are handcrafted (not data-driven) and therefore do not adequately make use of the prior knowledge of images, as described before. To overcome these problems, it unsurprisingly motivates us to seek for the data-driven BCS strategy, that is, learning BCS from a set of training data. To this end, one should center on the following questions:

- Can we design a learning-based image acquisition without handcrafting both the sparsifying domain and the sensing operator?
- With the data-dependant acquisition, is there any possibility that we can customize non-iterative reconstruction algorithms for BCS?
- How does the performance of the data-driven BCS compare to that of the state-of-the-art algorithms?

These questions naturally guide us to incorporate the deep learning (DL) concept in BCS. Roughly speaking, DL is a framework for automating feature learning and extracting, which has broadly used in computer vision tasks. Inspired by this technique, different attempts have been exploited to adopt the DL concept to CS imaging. For one thing, improvements

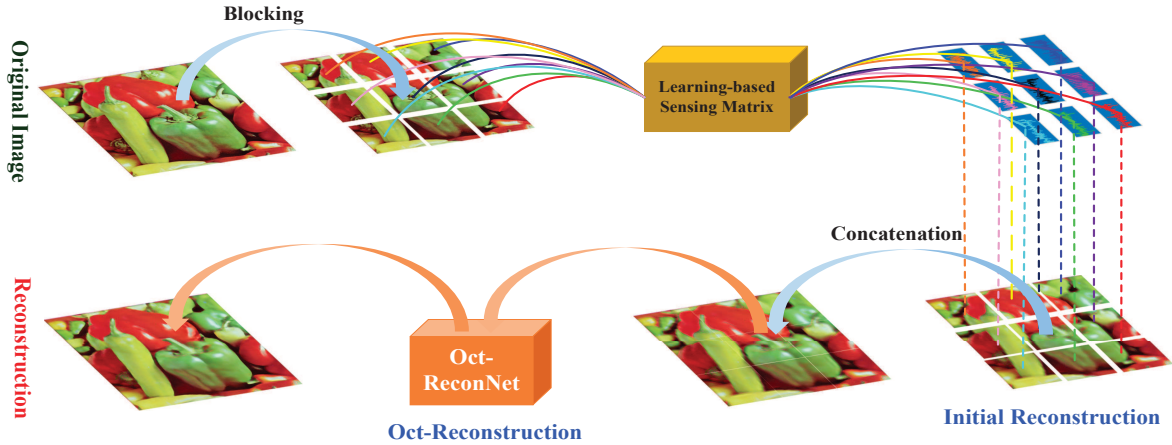


Fig. 1: Schematic representation of our proposed AutoBCS architecture. AutoBCS replaces the traditional BCS approach with a unified image acquisition and reconstruction framework.

to iterative algorithms using DL technique like ADMM-CSnet [37] and ISTA-net [38] have been introduced for image reconstruction, however, these frameworks still employ the traditional sensing operator and thus the data acquisition are signal independent. For another thing, the block-based reconstruction networks for BCS such as ReconNet [39] and DR²-net [40] have been developed, nevertheless, these networks only utilize intra-block information to recover a sub-block thereby yielding heavy blocking artifacts, and thus requiring a postprocessing algorithm. And thirdly, the pure DL-based BCS pipelines [41–43] have been proposed, unfortunately, existing frameworks usually use the undesirable fully connected network, and they are not fully recognized in theoretical analysis.

B. Main contributions

To address the previously described problems, motivated by the perceptual learning archetype, we propose a pure DL-based framework for BCS from data acquisition to reconstruction in this paper. Figure 1 shows the schematic representation of our proposed AutoBCS architecture, which replaces the traditional BCS approach, with a unified image acquisition and reconstruction framework. The main contributions are summarized as follows:

- We build a bridge between traditional non-learning strategies and prior knowledge from training sub-block image sets and develop a learning-based sensing matrix (LSM) for image acquisition, therefore without handcrafting the sparsifying domain and the sensing operator.
- The generated LSM is proved to satisfy the theoretical guarantees, such as RIP, and thus can be applied to the traditional BCS framework while the sampling efficiency can be significantly improved.
- We develop a non-iterative image reconstruction strategy mainly relying on our customized octave reconstruction, which establishes an end-to-end BCS reconstruction to eliminate blocking artifacts and maximize image reconstruction accuracy, in the proposed AutoBCS architecture.

The experimental results on several public testing databases all demonstrate that, compared with the other state-of-the-art

approaches, our AutoBCS framework can not only provide superior performance in both image quality metrics (PSNR and SSIM) and visual perception, but also automatically benefit reconstruction speed.

The rest paper is organized as follows. In Section II, we briefly review the related works to highlight our motivations. Section III describes our AutoBCS framework in detail. Extensive experiments are derived in Section IV to present the superiorities and effectiveness of the proposed framework. Section V demonstrates the relevant discussion and we conclude this paper in Section VI.

II. RELATED WORK

In this section, we will review some related works on both traditional block-based and DL-based image compressive sensing via a general insight to highlight our motivations and contributions, and simultaneously introduce the octave convolution.

A. Traditional block-based image compressive sensing

Considering a full-size image \mathbf{x} of $n = H \times W$ pixels, BCS divides \mathbf{x} into non-overlapping sub-block images with size $A \times A$ and measure each sub-block using the same sensing operator. Let \mathbf{x}_i denote the vectorized vector of the i^{th} sub-block in raster-scan manner. Using an $m_a \times A^2$ sensing matrix \mathbf{B}_A , we can obtain the corresponding measurements \mathbf{y}_i via

$$\mathbf{y}_i = \mathbf{B}_A \mathbf{x}_i. \quad (4)$$

Such a way is equivalent to apply general-purpose CS to the whole image \mathbf{x} by using a block diagonal sensing operator \mathbf{B} defined as:

$$\mathbf{B} = \begin{pmatrix} \mathbf{B}_A & 0 & \cdots & 0 \\ 0 & \mathbf{B}_A & \cdots & 0 \\ \vdots & \vdots & \ddots & \vdots \\ 0 & 0 & \cdots & \mathbf{B}_A \end{pmatrix}. \quad (5)$$

Note that $m_a = \lfloor \frac{mA^2}{n} \rfloor$ and the sampling rate is $\tau = \frac{m}{n}$, where m is the total number of the measurements \mathbf{y} through \mathbf{B} .

As an inspiring work, Gan et. al [26] used linear MMSE estimation as criterion to obtain initial solution, and then employed two-stage iterative hard thresholding to further improve the quality of initial image. Following this baseline framework, Mun et. al [32] then developed a better image reconstruction strategy for BCS, dubbed D-SPL, which combines SPL with direction transforms to simultaneously benefit smoothness and sparsity. It suggests that the dual-tree discrete wavelet transform (DWT) and contourlets can provide the better reconstruction performance at low sampling rates. An improvement to this method, which utilizes multiple scales and sub-bands of DWT, was proposed by Fowler et.al in [33]. After that, they used a multi-hypothesis prediction to develop a different BCS strategy, dubbed MH-SPL, for images and videos [36]. For still image, MH-SPL first calculates a multiple prediction of a sub-block image from spatially surrounding sub-blocks as an initial reconstruction and then obtains the final prediction of the sub-block through an optimal linear combination. For video, MH-SPL can obtain the corresponding multi-hypothesis prediction of a frame from previously recovered adjacent frames. Comprehensive reviews on this kind of BCS method and its applications can be found in [44]. Moreover, block/patch-based methods that enforce the nonlocal self-similarity and local sparsity, such as RCoS [34] and GBsR [35], were developed for natural image. These aforementioned approaches can always obtain a higher-quality image but with a low reconstruction speed.

In a nutshell, the traditional BCS strategies generally enhance the performance by mainly designing the sparsifying domain or exploiting the prior knowledge of the image. Different from them, our method is a pure data-driven BCS framework from image acquisition to reconstruction. Compared with traditional BCS paradigm, our data-driven method automatically learns the features of each sub-block image and the relationship among sub-blocks and develops a learning-based sensing matrix from training data to obtain image acquisition. In addition, the proposed AutoBCS can provide better image recovery accuracy with an extremely fast recovery speed.

B. Deep learning-based image compressive sensing

To substitute the traditional iterative reconstruction approaches, several attempts have been devoted to adopt the DL technique to CS imaging. Roughly speaking, we can divide these DL-based BCS frameworks into three categories. First of all, interpretable optimization-inspired image reconstruction strategies have been developed by casting iterative optimization algorithms into DL form, in which the involved parameters are not hand-crafted, but being gradually learned end-to-end. For example, Yang et. al [37] introduced an effective iterative deep architecture, called ADMM-CSnet, which is inspired by the iterative ADMM solver for solving Eq. (3). Based on ISTA solver, similarly, Jian et. al [38] developed ISTA-net to solve the proximal mapping related to the sparsity-inducing regularizer, which indeed improves the recovery performance. Nevertheless, these frameworks mainly focus on learning the sparsifying domain and reconstruction

strategy without concerning the sensing operator, and thus the data acquisition are not data-dependant, which may weaken the CS performance.

In the second place, learning block-based image reconstruction networks have been designed for CS imaging. At the beginning, Mousavi et. al [45] applied a stacked denoising autoencoder non-iterative network (SDA-net) to reconstruct the image from its measurements. Following this work, Kulkarni et. al [39] and Yao et. al [40] respectively developed two non-iterative reconstruction frameworks, known as ReconNet and DR²-net, by borrowing insights from traditional BCS reconstruction methods, which have competitive reconstruction performance with a significantly short recovery speed. However, such non-iterative reconstruction networks usually have two deficiencies. For one thing, these non-iterative networks only employ intra-block information to recover a sub-block image thereby yielding blocking artifacts, and thus requiring an addition de-blocking algorithm with high computational complexity. For another, the involved sensing matrix for image acquisition is hand-crafted as well, i.e., these networks still do not take into account the sampling patterns of data acquisition.

To address these problems, finally, the pure DL-based BCS pipelines [41–43] have been proposed for CS imaging, which train a non-iterative reconstruction network associated with learning the sampling patterns. For example, Wu et. al [42] introduced a BCS framework, called CS-net, for jointly optimizing the sampling patterns and the reconstruction strategy via convolutional neural network, which was further extended in [43]. In their research, CS-net can provide substantial improvements on reconstruction accuracy than other algorithms, with a fast running speed. However, the existing pure DL-based BCS frameworks still suffer from many disadvantages, such as less theoretical or comprehensive analysis, using the undesirable fully connected or repetitive network, and etc., which may hinder their practical applications.

Fundamentally, our proposed AutoBCS is a pure DL-based BCS framework, which utilizes networks to learn mapping between a set of measurements obtained by LSM and high-quality image. Although both our proposed AutoBCS and other pure DL-based ones have similar inspirations, they are different due to the following reasons. On one hand, our framework not only learns the prior information of images, but also develops LSM for image acquisition. The generated LSM is proved to satisfy the theoretical guarantees of the sampling patterns. On the other hand, existing reconstruction networks generally use either fully connected or repetitive convolutional layer to accomplish image reconstruction, while our customized non-iterative reconstruction module in AutoBCS goes beyond that to consistently boost accuracy for image, reducing computational complexity and memory cost.

C. Octave convolution

In convolutional neural networks, we can consider the output feature maps of a convolution layer as a mixture of information at multiple spatial frequencies. Octave convolution introduced by Chen et. al [46] is a novel frequency decomposition of convolution operation, which stores and processes

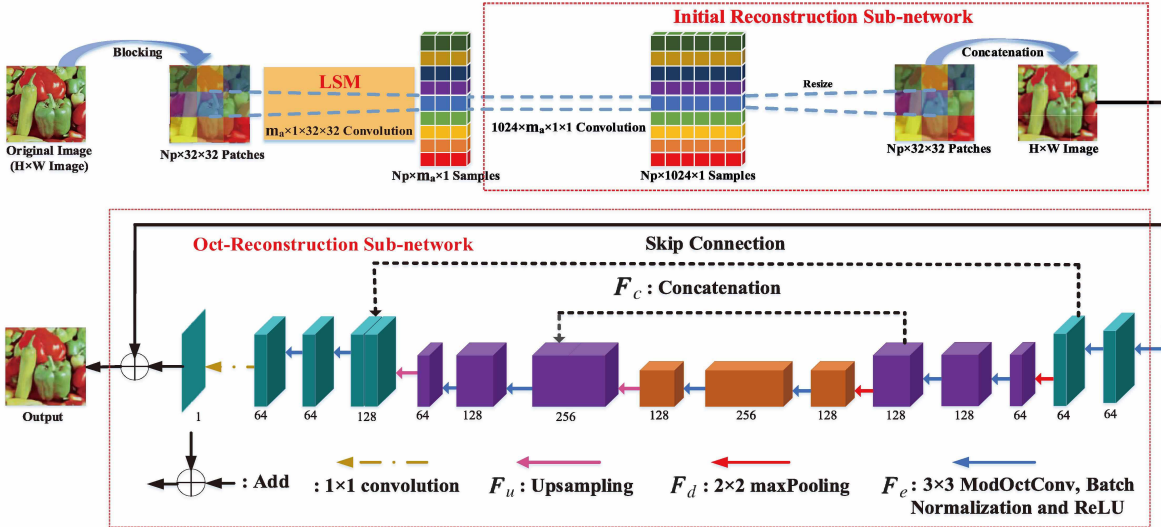


Fig. 2: The deep neural network architecture of AutoBCS contains two parts: data-driven image acquisition module and non-iterative data reconstruction module. Note that we use different colors for the corresponding block processing to distinguish different sub-block images.

the mixed feature maps, while decreasing spatial redundancy. As an alternative of vanilla convolutions, it is a kind of plug-and-play convolutional operator, and can effectively reduce the resolution for low frequency maps and enlarge the receptive field, and thus saving both computation and storage. With achieving significant performance gain, octave convolution is perfectly suitable for a variety of backbone deep convolutional networks related to image and video processing tasks, such as Res2Net [47] and stabilizing GANs [48], without any adjustment on the backbone network architecture.

For the sake of augmenting the detail recovery and maximizing image reconstruction accuracy, we specially modify the original octave convolution and customize an octave transposed convolution to make the octave idea more suitable for our non-iterative reconstruction network in this work. The related details about modified octave convolution and octave transposed convolution are introduced in Appendix A, Part I and Part II, respectively. Compared with general DL-based ones, our customized octave reconstruction strategy does not contain fully connected or repetitive network, nor does it require de-blocking processing.

III. PROPOSED METHOD

In this section, we will develop a pure DL-based BCS framework with data-driven image acquisition and non-iterative data reconstruction to solve the questions mentioned in Section I, that is, how to efficiently measure image without handcrafting both the sparsifying domain and the sensing operator for better sampling; how to use non-iterative reconstruction network to reconstruct image for better recovery accuracy.

A. Framework of AutoBCS

The proposed AutoBCS is a pure DL-framework incorporating data-driven image acquisition and reconstruction mod-

ules, as described in Fig. 2. In the data acquisition module, AutoBCS automatically captures the features of each block image and the relationship among sub-block images and correspondingly develops a learning-based sensing matrix (LSM) from training data. In the image reconstruction module, AutoBCS learns a reconstruction mapping between a set of measurements obtained by LSM and high-quality images. As the mapping is made, a low-dimensional and mutual joint manifold of these two types of data is implicitly learned, seizing an extremely expressive representation which maximizes image reconstruction accuracy. To be specific, the non-iterative reconstruction module used in AutoBCS includes two phases: initial reconstruction sub-network and octave reconstruction sub-network. The former aims to obtain an initial recovery image with the global structure while the latter focuses on augmenting fine details and finally outputs a high-quality reconstruction image.

For data training, the image acquisition module and the reconstruction module in AutoBCS are jointly optimized, and form an end-to-end network in order to maximize both sampling efficiency and recovery performance. For application implementation, the trained LSM is utilized to yield a set of measurements for each sub-block, and equivalently forms a block-diagonal matrix with constrained structure for encoding the full-size image to obtain image acquisition. Moreover, the trained non-iterative reconstruction module is considered as a decoder to accomplish image reconstruction.

B. Data-driven image acquisition module

As described in Eq. (4), the traditional BCS employs \mathbf{B}_A to respectively obtain a set of measurements \mathbf{y}_i from each sub-block image \mathbf{x}_i . In our AutoBCS, a convolutional layer with kernel size (A) and stride (A) and zero bias is used to implement the linear non-overlapping block-based sampling stage, as each row of \mathbf{B}_A can be considered as a filter. More

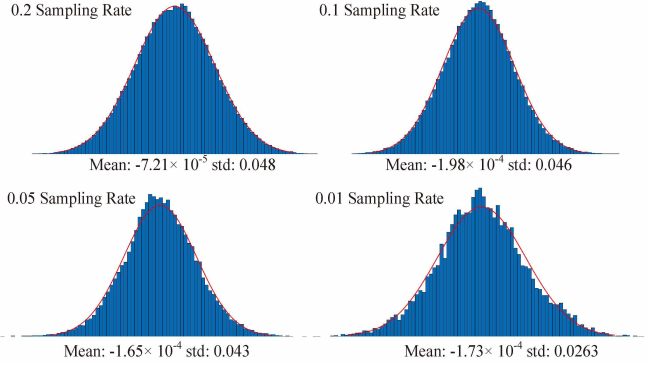


Fig. 3: Histograms of the element distribution of \mathbf{P}_A in the cases: (a) $\tau = 0.2$; (b) $\tau = 0.1$; (c) $\tau = 0.05$; (d) $\tau = 0.01$, respectively, where the red line corresponds to standard Gaussian distribution.

specifically, the image acquisition of AutoBCS is shown in the upper left part of Fig. 2, where N_p denotes the total number of sub-block images, and the size of each filter used in sampling layer is the same as that of sub-block image, i.e., $A \times A^1$. At a sampling rate $\tau = \frac{m}{n}$, the sensing matrix \mathbf{B}_A has $m_a = \lfloor \frac{mA^2}{n} \rfloor$ rows for image acquisition. As a consequence, the convolution layer has m_a filters of size $A \times A$ to obtain m_a measurements. For example, if $\tau = 0.01$, there are 10 filters of size 32×32 in the sampling layer.

To be more formal, let \mathbf{F}_A represent m_a filters of the sampling convolution layer. Mathematically, the non-overlapping block-based image acquisition can be formulated as a convolution operation:

$$\mathbf{y}_i = \text{conv}(\mathbf{F}_A, \mathbf{x}_i) = \mathbf{F}_A * \mathbf{x}_i, \quad (6)$$

which corresponds to the sampling procedure of traditional BCS described by Eq. (4). When inputting an sub-block image \mathbf{x}_i to the sampling layer, the output \mathbf{y}_i is a vector of size m_a , which can be considered as the corresponding measurements of \mathbf{x}_i . In AutoBCS architecture, the sampling layer automatically learns the sampling patterns from the training data, i.e., the weights of \mathbf{F}_A are gradually optimized for better data acquisition. Once the training is completed, we can obtain the corresponding LSM, denoted by \mathbf{P}_A . LSM can naturally capture the features of each sub-block image and the relationship among sub-blocks, and thus can guarantee that \mathbf{y}_i inherits more structural characteristic of \mathbf{x}_i .

In order to analyse the property of \mathbf{P}_A , we have trained four AutoBCS networks at four sampling rates, i.e., $\tau \in \{0.2, 0.1, 0.05, 0.01\}$. The training details will be introduced in Section V. To this end, Fig. 3 plots the element distribution of the trained \mathbf{P}_A for visualization, where the red line corresponds to standard Gaussian distribution. From these histograms, it can be distinctly observed that the elements of \mathbf{P}_A , $P_{k,j}$ ($1 \leq k \leq m_a, 1 \leq j \leq A^2$) indeed obey Gaussian-like distribution, especially for AutoBCS with higher τ .

Although the elements of LSM and Gaussian matrix meet a similar distribution, they are totally diverse in essence

¹As done in other BCS frameworks, we employ block of size $A = 32$ in our work.

because of the following two aspects. Firstly, Gaussian matrix in traditional framework is usually handcrafted without considering the prior information of the data, while our LSM is fundamentally learned according to the prior knowledge, rather than manually set. Secondly, the statistical properties of elements of Gaussian matrix, such as mean and variance, are fixed and signal independent, while these characteristics of elements of LSM are gradually optimized from training data to improve the sampling efficiency. Roughly speaking, we can consider that \mathbf{P}_A is automatically learned from the training data, whose elements follow a Gaussian-like distribution.

As described before, random matrices based on Gaussian, Bernoulli or more generally a Gaussian-like distribution [22] have been shown to perfectly promote the theory of CS to satisfy real-world data acquisition demands. As a consequence, we can leverage the well-known theorems on random matrices to obtain many interesting conclusions for our trained LSM, coming with theoretical guarantees. For brevity, we present the details in Appendix B. In another viewpoint, for the full-size image \mathbf{x} , the equivalent sensing operator \mathbf{P} can be considered to follow the form of Eq. (5) with constant block diagonal element \mathbf{P}_A . As might be expected, the equivalent block sensing matrix \mathbf{P} follows the RIP- or coherence-based performance guarantees as well. More related theoretical details on block diagonal matrices can be found in [49, 50] and the references therein.

In short, the trained LSM implicitly learns the structural characteristic of images, and meets asymptotically optimally theoretical guarantees. As a result, the proposed AutoBCS is data-driven, which will automatically benefit the image acquisition.

C. Non-iterative data reconstruction module

We implement our non-iterative image reconstruction module with a deep neural network architecture consisted of an initial reconstruction sub-network followed by an octave reconstruction sub-network.

1) *Initial reconstruction sub-network*: Using linear MMSE estimation as optimization criterion, the traditional BCS frameworks [26] utilized an $A^2 \times m_a$ reconstruction matrix $\hat{\mathbf{B}}_A = \rho_{\mathbf{x}_i, \mathbf{x}_i} \mathbf{B}_A^T (\mathbf{B}_A \rho_{\mathbf{x}_i, \mathbf{x}_i} \mathbf{B}_A^T)^{-1}$ to obtain initial reconstructed image, i.e., $\hat{\mathbf{x}}_i = \hat{\mathbf{B}}_A \mathbf{y}_i$, where $\hat{\mathbf{x}}_i$ is the reconstructed vector of the i^{th} sub-block image and $\rho_{\mathbf{x}_i, \mathbf{x}_i}$ denotes the autocorrelation function of the input data. As a replacement to the reconstruction matrix, a convolutional layer with 1024 kernels of size 1×1 and no bias terms is used to perform the initial reconstruction in our AutoBCS. It is noticed that the initial reconstruction sub-network is a linear signal reconstruction layer, as there is no activation function and bias.

Similar to the data acquisition, we can also formulate the initial reconstruction as a convolution operator:

$$\hat{\mathbf{x}}_i = \text{conv}(\mathbf{F}_{int}, \mathbf{y}_i) = \mathbf{F}_{int} * \mathbf{y}_i, \quad (7)$$

where $\hat{\mathbf{x}}_i$ denotes the initial reconstruction vector of \mathbf{x}_i and \mathbf{F}_{int} represents A^2 filters of size 1×1 in the initial reconstruction layer. Obviously, $\hat{\mathbf{x}}_i$ is a $1 \times A^2$ vector. The traditional BCS strategies always resize and concatenate these reconstruction

vectors obtained by reconstruction matrix to gain the initial reconstruction result of \mathbf{x} . Following this baseline framework, we first resize each $1 \times A^2$ reconstruction vector $\widehat{\mathbf{x}}_i$ to an $A \times A$ sub-block result, and then concatenate all sub-blocks to obtain an initial reconstruction image $\widehat{\mathbf{x}}$ in our AutoBCS. Let $\gamma(\cdot)$ and $\zeta(\cdot)$ denote the reshape operator and the corresponding concatenation, respectively. We can formulate the following model:

$$\widehat{\mathbf{x}} = \zeta \begin{pmatrix} \gamma(\widehat{\mathbf{x}}_{11}) & \gamma(\widehat{\mathbf{x}}_{12}) & \cdots & \gamma(\widehat{\mathbf{x}}_{1c}) \\ \gamma(\widehat{\mathbf{x}}_{21}) & \gamma(\widehat{\mathbf{x}}_{11}) & \cdots & \gamma(\widehat{\mathbf{x}}_{2c}) \\ \vdots & \vdots & \ddots & \vdots \\ \gamma(\widehat{\mathbf{x}}_{r1}) & \gamma(\widehat{\mathbf{x}}_{r2}) & \cdots & \gamma(\widehat{\mathbf{x}}_{rc}) \end{pmatrix}, \quad (8)$$

where r and c jointly denote the positions of the sub-block images in the original full-size image.

In fact, only exploiting the initial reconstruction sub-network is not sufficient because the sub-block image quality of the initial recovery is low and the concatenation operator will always yield blocking artifacts in the space domain. For the sake of exact reconstruction, we develop a customized octave reconstruction sub-network, which can automatically draw on the information of both intra- and inter- sub-block images, to eliminate blocking artifacts and maximize image reconstruction accuracy.

2) *Octave reconstruction sub-network*: As shown in the bottom part of Fig. 2, an octave convolution modified U-net architecture is introduced to further improve the reconstruction quality of \mathbf{x} . Similar to traditional U-net [51], our proposed octave reconstruction sub-network consists of a contracting path and an expanding path as well. The goal of the former is to produce high-dimensional features from the local receptive field. Thus, this part could be considered as feature extraction part, which is a set of octave-convolution and max-pooling operations (two convolutions followed by one max-pooling). For the contracting path, two separate operations \mathbf{F}_e and \mathbf{F}_d (denoted by the blue and red arrows in Fig. 2, respectively) are involved and can be summarized as:

$$\mathbf{F}_e(\widehat{\mathcal{X}}) = \text{ReLU}(\text{ModOctConv}(\widehat{\mathcal{X}}, 3) + z), \quad (9)$$

$$\mathbf{F}_d(\widehat{\mathcal{X}}) = \text{MaxPool}(\widehat{\mathcal{X}}, 2), \quad (10)$$

where $\widehat{\mathcal{X}}$ is the input feature maps, and $\text{ModOctConv}(\cdot, 3)$ denotes the 3×3 modified octave convolution operation designed in Appendix A, Part I, z is the bias of this layer, $\text{ReLU}(\cdot)$ represents one of the most common activation function (Rectified linear unit, $\max(0, x)$), $\text{MaxPool}(\cdot, 2)$ is the 2×2 max-pooling operation.

The design of the upsampling-path is to increase the resolution of the images to the original size, and more importantly, such a U-shape design allows the network to perform convolution on feature maps at different spatial resolution, resulting in a multi-scale feature representation with enlarged receptive fields. Thus the first operation in this part is a transposed convolution to increase the resolution of the feature maps gradually to the original size. This operation \mathbf{F}_u , denoted by purple arrow in Fig. 2, is included to oppose the effects of pooling layers, and it can be expressed as:

$$\mathbf{F}_u(\widehat{\mathcal{X}}) = \text{ReLU}(\text{OctTransConv}(\widehat{\mathcal{X}}, 2) + z), \quad (11)$$

where $\text{OctTransConv}(\cdot, 2)$ represents the 2×2 octave transposed convolution introduced in Appendix A, Part II.

Immediately after these transposed operations, some concatenations between layers of contracting path and expanding path are introduced to compensate the potential spatial loss during the down-sampling path. We can formulate the concatenation \mathbf{F}_c , denoted by black dash arrow in Fig. 2, as:

$$\mathbf{F}_c(\widehat{\mathcal{X}}_1, \widehat{\mathcal{X}}_2) = \text{MatrixCat}(\widehat{\mathcal{X}}_1, \widehat{\mathcal{X}}_2), \quad (12)$$

where $\widehat{\mathcal{X}}_1$ and $\widehat{\mathcal{X}}_2$ denote the corresponding feature maps of the layers of contracting path and expanding path, respectively. For example, if the sizes of matrices $\widehat{\mathcal{X}}_1$ and $\widehat{\mathcal{X}}_2$ are $256 \times 256 \times 10$ and $256 \times 256 \times 20$, respectively, then the output will be a matrix of size $256 \times 256 \times 30$.

Finally, a skip connection between the initial reconstruction result and the final output forms a residual block and can help the training convergence more easily. Therefore, the final reconstructed image $\tilde{\mathbf{x}}$ can be obtained by:

$$\tilde{\mathbf{x}} = \widehat{\mathbf{x}} + \text{OctReconNet}(\widehat{\mathbf{x}}), \quad (13)$$

where $\text{OctReconNet}(\widehat{\mathbf{x}})$ denotes the output of the octave reconstruction sub-network.

D. Loss Function

The proposed AutoBCS is a pure DL-based BCS framework from image acquisition to reconstruction. Given an input image \mathbf{x} , our aim is to estimate parameters \mathbf{W} of AutoBCS such that it can automatically and efficiently obtain samples \mathbf{y} via image acquisition module, and then rapidly and exactly reconstruct \mathbf{x} from \mathbf{y} through data reconstruction module. To achieve this goal, we take the original image \mathbf{x} as the ground truth and the corresponding reconstruction image $\tilde{\mathbf{x}}$ generated by AutoBCS as output. Specially, we design two loss functions. One is for training the whole AutoBCS, and the other is for the initial reconstruction sub-network. For the the whole AutoBCS, the loss function is

$$\mathcal{L}(\mathbf{W}) = \frac{1}{2N} \sum_{j=1}^N \|\text{AutoBCS}(\mathbf{x}^j; \mathbf{W}) - \mathbf{x}^j\|_2^2, \quad (14)$$

where N is the number of the training images, \mathbf{x}^j denotes the j^{th} original image, and $\text{AutoBCS}(\mathbf{x}^j; \mathbf{W})$ represents $\tilde{\mathbf{x}}^j$. For the initial reconstruction sub-network, the loss function is

$$\mathcal{L}_{int}(\mathbf{W}_{int}) = \frac{1}{2N} \sum_{j=1}^N \|I(\mathbf{x}^j; \mathbf{W}_{int}) - \mathbf{x}^j\|_2^2 \quad (15)$$

where \mathbf{W}_{int} and $I(\mathbf{x}^j; \mathbf{W}_{int})$ represents the parameters and the output of the initial reconstruction sub-network. Note that the image acquisition and reconstruction modules are jointly trained, which impels AutoBCS to overcome the two main challenges of CS theory.

IV. EXPERIMENTAL VALIDATION

The proposed AutoBCS will be verified with extensive experiments in this section. In addition, we will compare our AutoBCS with conventional BCS methods including TAL3 [52], D-SPL [32], MH-SPL [36], RCoS [34] and GBsR [35],

TABLE I: AutoBCS vs. different conventional BCS methods on three typical benchmark databases

Databases	Sampling rate τ	TAL3		D-SPL		MH-SPL		RCoS		GBsR		AutoBCS	
		SSIM	PSNR	SSIM	PSNR								
Set5	0.01	0.4553	15.51	0.1387	9.27	0.4352	18.01	0.4684	18.35	0.4901	18.78	0.6696	24.25
	0.04	0.5121	19.98	0.2773	12.71	0.6101	22.50	0.6358	23.11	0.6888	23.82	0.8446	29.18
	0.1	0.7855	26.85	0.7641	24.66	0.8217	28.63	0.8522	29.56	0.8679	30.12	0.9190	33.28
	0.25	0.8903	31.57	0.8939	32.64	0.9055	33.20	0.9273	34.13	0.9401	35.72	0.9607	37.65
	0.3	0.9008	32.68	0.9062	33.66	0.9164	34.08	0.9331	35.06	0.9496	36.89	0.9675	38.75
	Avg.	0.7088	25.32	0.5960	22.58	0.7378	27.28	0.7634	28.04	0.7873	29.07	0.8723	32.62
Set14	0.01	0.3989	15.26	0.0978	8.95	0.4211	17.22	0.4274	17.56	0.4330	17.81	0.5968	23.12
	0.04	0.5083	19.37	0.2170	12.91	0.5345	21.02	0.5686	21.73	0.5849	22.32	0.7348	28.67
	0.1	0.6883	25.21	0.6908	24.27	0.7492	26.88	0.7612	27.13	0.7954	28.24	0.8343	29.56
	0.25	0.8131	29.01	0.8264	29.71	0.8645	31.20	0.8836	31.86	0.9017	32.65	0.9205	33.67
	0.3	0.8422	30.08	0.8482	30.68	0.8824	32.06	0.8910	32.65	0.9092	33.70	0.9347	34.81
	Avg.	0.6502	23.79	0.5360	21.30	0.6903	25.68	0.7064	26.18	0.7248	26.94	0.8042	29.97
BSD100	0.01	0.3991	15.97	0.1065	9.65	0.4016	18.06	0.4258	18.31	0.4438	18.64	0.5578	23.79
	0.04	0.4473	18.10	0.2201	13.30	0.4954	20.89	0.5187	21.48	0.5390	22.12	0.6833	26.40
	0.1	0.6610	25.42	0.6341	23.45	0.6669	25.17	0.6817	25.45	0.7048	25.88	0.7937	28.74
	0.25	0.7872	28.41	0.7811	28.25	0.8026	28.90	0.8234	29.63	0.8432	30.21	0.9019	32.33
	0.3	0.8188	29.13	0.8086	29.20	0.8305	29.85	0.8445	30.23	0.8632	30.90	0.9215	33.39
	Avg.	0.6227	23.41	0.5101	20.77	0.6394	24.57	0.6588	25.02	0.6788	25.55	0.7716	28.93



Fig. 4: Sample images from BSD500 database.

and the newly-developing DL approaches including SDA-net [45], ReconNet [39], DR²-net [40], ISTA-net [38], and CS-net [43]. Similar to our AutoBCS, the block size for these state-of-the-art frameworks is set to $A = 32$ as well. The structural similarity index (SSIM) and the peak signal-to-noise ratio (PSNR in dB) [53] are used to evaluate the reconstruction accuracies of network performance.

A. Training Details

1) *Implementation*: The implementation of the proposed AutoBCS model has been done using Pytorch 1.0 Framework on 2 TeslaV100 GPUs.

2) *Experimental data*: Our training dataset is composed of 400 images drawn from the popular database BSD500 [54], namely 200 train images and 200 test images. Some sample images for training are illustrated in Fig. 4. In order to improve the network performance, data augmentation including image flipping, rotating and their combination [55] are also applied to account more detail cases of recovery images. In total, the training images are prepared as 89600 sub-images (96×96 pixel size), with mini-batch size of 64, for network training. We train the proposed AutoBCS model for 100 epoches, while the learning rate is scheduled as 10^{-3} for the first 50 epochs, 10^{-4} for 51-80 epochs, and 10^{-5} for final 20 epochs. In addition, five well-known datasets including Set5

[56], Set11 [39], Set14 [57], BSD68 and BSD100 [58], are utilized as test data to increase the diversity and generality of the benchmark. To facilitate visual perception, we only exploit grayscale information of images for both training and testing, as in other BCS approaches.

B. Comparisons with traditional BCS methods

In this part, the superiorities and effectiveness of the proposed AutoBCS are validated by comparing with five conventional BCS methods, namely TAL3, D-SPL, MH-SPL, RCoS, and GBsR, on three typical benchmark databases including Set5, Set14 and BSD100. For these conventional algorithms, we use the default setups declared in the author's websites, and run them on an Intel(R) Core(TM) i7-4770 CPU @ 3.40 GHz with RAM 16.0 GB. The comparison results of SSIM and PSNR for the aforementioned approaches are illustrated in Table I and the best result for each unit, here and after, will be marked in boldface. In an overall view, it can be observed that our proposed AutoBCS obtains the best performance in both SSIM and PSNR on the three databases than all compared conventional BCS methods. Even comparing with the best traditional algorithm GBsR, our AutoBCS can enhance SSIM on average by approximately 33.46%, 24.82%,

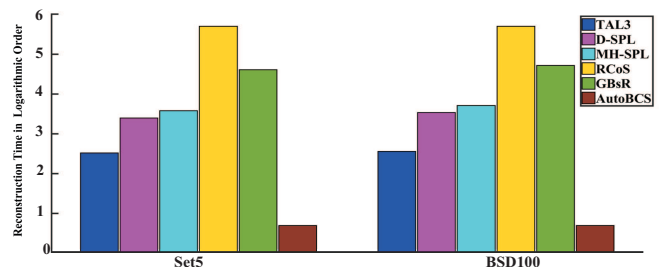


Fig. 5: Comparison of reconstruction time in logarithmic order for traditional BCS methods and AutoBCS on the Set5 and BSD100. Please zoom in for better comparison.

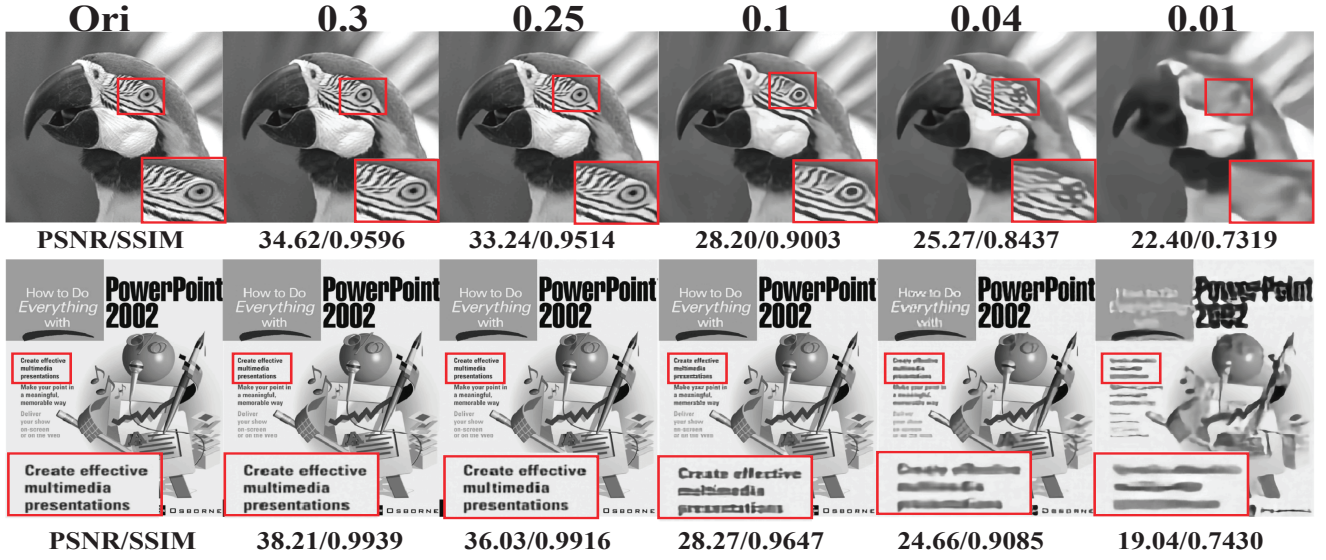


Fig. 6: Illustration of reconstructed images by using AutoBCS at different sampling rates. The first column: original image; the reconstruction columns for left to right correspond to $\tau = 0.3$, $\tau = 0.25$, $\tau = 0.1$, $\tau = 0.04$, and $\tau = 0.01$, respectively. Please zoom in for better comparison.

7.55%, 3.65%, and 3.74% at different sampling rates, where $\tau \in \{0.01, 0.04, 0.1, 0.25, 0.3\}$, and the PSNR improvements are about 5.31 dB, 5.33 dB, 2.45 dB, 1.69 dB, and 1.82 dB, respectively. From these results, obviously, our proposed AutoBCS has great benefits at all sampling rates. Although the sampling rate is 0.01, particularly, our method still provides superior performance in terms of both SSIM and PSNR. Moreover, we plot the comparison of recovery time on the databases Set5 and Set14 in the case of $\tau = 0.1$. Please refer to Fig. 5, where the vertical axis obeys $t = 2 + \log_{10}(t_{real})$ (t_{real} represents real recovery time). For example, the real reconstruction time of AutoBCS $t_{real} = 0.04$ ms, then $t = 0.60$. Inspecting the figures, it can be concluded that, our proposed AutoBCS reduces the recovery time by a large margin and outperforms the other traditional BCS algorithms in all cases. Even comparing with the fastest traditional BCS algorithm TAVL3, AutoBCS is three orders of magnitude faster in recovery speed.

In addition, we visualize the reconstructed images in order to facilitate visual comparison. Figure 6 illustrates the corresponding reconstructed images for AutoBCS at τ from 0.01 to 0.3. It once again verifies that AutoBCS can still contain rich semantic content even at a particularly low sampling rate. As a

consequence, our proposed AutoBCS is extraordinarily desirable for low-power imaging devices. Finally, Fig. 7 depicts the comparison of the reconstructed images at various sampling rates. From these visual illustrations, we can evidently observe that AutoBCS is superior to the traditional BCS methods, especially in recovering detail and texture.

In summary, our proposed AutoBCS can improve the performance in both reconstruction accuracy and recovery speed, and bring about better results than the conventional BCS methods in different cases on these public benchmark datasets.

C. Comparisons with DL-based BCS methods

In this part, several DL-based BCS methods, namely SDA-net, ReconNet, DR²-net, ISTA-net, and CS-net, are compared with our AutoBCS to further demonstrate the effectiveness of the proposed approach. Following the previous work [38], we select dataset Set11 and BSD68 for testing, and summarize the comparison result of PSNR for these approaches in Table II and Table III, respectively. For fair comparison, the listed results are achieved from the corresponding works or reproduced as stated in the optimal setting provided by the corresponding papers. The denoising postprocessing operator of SDA, ReconNet and DR²-net, i.e., BM3D denoiser, is also

TABLE II: Average PSNR (dB) comparison for AutoBCS and various DL-based BCS methods on Set11

Alg.	Sampling rate τ					
	0.01	0.04	0.1	0.25	0.3	Avg.
SDA-net	17.29	20.12	22.65	25.34	26.63	22.41
ReconNet	17.27	20.63	24.28	25.60	28.74	23.30
DR ² -net	17.35	21.14	24.98	25.87	29.12	23.69
ISTA-net	17.30	21.23	25.80	31.53	32.91	25.75
CS-net	20.94	24.91	28.10	32.12	33.86	27.99
AutoBCS	21.05	25.38	28.78	33.72	35.17	28.82

TABLE III: Average PSNR (dB) comparison for AutoBCS and various DL-based BCS methods on BSD68

Alg.	Sampling rate τ					
	0.04	0.1	0.3	0.4	0.5	Avg.
SDA-net	21.32	23.12	26.38	27.41	28.35	25.32
ReconNet	21.66	24.15	27.53	29.08	29.86	26.46
DR ² -net	21.87	24.34	27.77	29.27	29.96	26.64
ISTA-net	22.12	25.02	29.93	31.85	33.60	28.50
CS-net	24.03	27.10	31.45	32.53	34.89	30.00
AutoBCS	25.12	27.46	32.18	34.23	36.34	31.07



Fig. 7: Comparison for reconstruction images for traditional BCS methods and AutoBCS at various sampling rates. The first to third rows correspond to $\tau = 0.1$, $\tau = 0.2$, and $\tau = 0.3$, respectively. Please zoom in for better comparison.

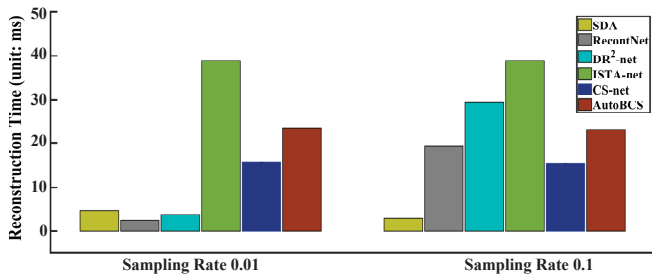


Fig. 8: Comparison of average reconstruction time (unit: ms) to reconstruct a 256×256 image for different DL-based BCS methods and AutoBCS on Set5 in case of $\tau = 0.01$ and $\tau = 0.1$.

considered, which can significantly enhance the reconstruction accuracies. As illustrated in Table II and Table III, we can make a conclusion that the proposed AutoBCS outperforms all the competitive DL-based methods in the case of these sampling rates. Let us check the recovery time for these approaches in the case of $\tau = 0.01$ and $\tau = 0.1$, which are shown in Fig. 8. We can evidently conclude that, compared with traditional BCS approaches, the DL-based BCS algorithms can achieve better performance, which verifies the superiorities of non-iterative reconstruction methods. Among the aforementioned DL-based approaches, our proposed AutoBCS obtains significantly better recovery accuracy with comparable reconstruction speed.

In particular, several visual comparisons of reconstructed images for $\tau = 0.1$ are illustrated in Fig. 9. By checking the figures, we empirically observe that the reconstruction images of SDA-net, ReconNet, and DR²-net have heavy

blocking artifacts. On the contrary, our proposed AutoBCS can smoothly reconstruct the image with more details and sharper edges. Overall, we can conclude from the results that AutoBCS have significantly improved the recovery performance in both quantitative validation and qualitative visualisation than other strategies being compared on the aforementioned databases.

V. DISCUSSION

In this section, we will firstly figure out LSM in comparative perspective to show whether it can indeed enhance sampling efficiency and then discuss whether our proposed AutoBCS is robust to noise.

A. LSM versus traditional sensing matrices

As previously described, we develop LSM for data-driven image acquisition in our proposed AutoBCS architecture. The generated LSM automatically captures the feature of each block image and the relationship among sub-block images, and is proved to satisfy the theoretical guarantees. As a consequence, LSM can significantly improve the sampling efficiency, and can be generally extended to the traditional BCS frameworks. To quantify the performance, we apply LSM and other four traditional sensing matrices (GSM [8], BSM [22], BcSM [28] and CbSM [26])² in the aforementioned BCS algorithms while other parameters remain unchanged. In case of $\tau = 0.1$ and database Set5, the corresponding results w.r.t both SSIM and PSNR are reported in Table IV. According to

²Note that GSM and BSM are two typical random sensing matrices, namely Gaussian and Bernoulli sensing matrices. BcSM is a widely used deterministic binary code-based sensing matrix [28]. CbSM represents Chebyshev chaotic binary matrix, which was introduced in [26].

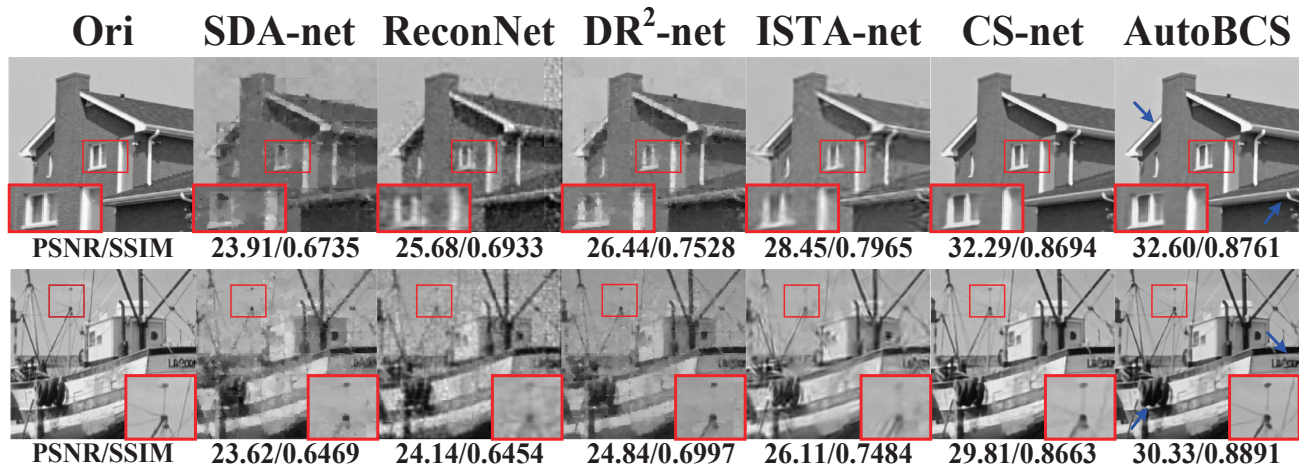


Fig. 9: Comparison for image reconstructions for various DL-based BCS approaches and AutoBCS at sampling rate $\tau = 0.1$. The reconstruction columns from left to right correspond to SDA-net, ReconNet, DR²-net, ISTA-net, CS-net and AutoBCS, respectively. Please zoom in for better comparison.

TABLE IV: Comparison results for various sensing matrices with traditional BCS methods at $\tau = 0.1$

Database	Sensing Matrix	TAL3		D-SPL		MH-SPL		RCoS		GBsR		Avg.	
		SSIM	PSNR										
Set5	GSM	0.7855	26.85	0.7641	24.66	0.8217	28.63	0.8522	29.56	0.8679	30.12	0.8183	27.96
	BSM	0.7786	26.76	0.7747	25.16	0.8202	28.56	0.8498	29.42	0.8624	29.86	0.8171	27.95
	BcSM	0.7858	26.97	0.7892	26.08	0.8238	28.81	0.8582	29.67	0.8701	30.34	0.8254	28.37
	CbSM	0.7781	26.73	0.7571	24.47	0.8176	28.40	0.8487	29.46	0.8608	29.73	0.8125	27.76
	LSM	0.8378	29.56	0.8375	29.86	0.8499	30.89	0.8908	31.79	0.9002	32.51	0.8632	30.92

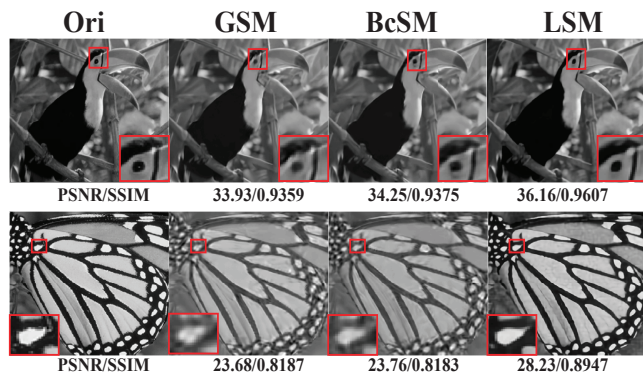


Fig. 10: Comparison of image reconstruction using three sensing matrices combined with traditional GBsR algorithm. First column: the original image; the reconstruction columns are based on GSM, BcSM and our trained LSM, respectively. Please zoom in for better comparison.

the comparison results, we can distinctly observe that these traditional BCS methods equipped with our generated LSM greatly enhance the sampling efficiency for better reconstruction, and they can improve the reconstruction accuracy by roughly 5.48% on SSIM and 10.39% on PSNR in average.

Let us now validate the comparison methods in visual sight to make it more convinced. We select “bird” and “butterfly” as the original images of interest. Following the previous setting, we show the comparison results in Fig. 10. From these visual

TABLE V: Average PSNR (dB) comparison of the competing approaches for various noise levels on dataset Set5

Noise	Alg.	Sampling rate τ				
		0.01	0.04	0.1	0.25	0.3
$\sigma_n = 0.01$	D-SPL	9.26	12.70	24.61	32.49	33.45
	MH-SPL	17.96	22.48	28.62	33.02	33.87
	GBsR	18.76	23.80	29.73	35.59	36.68
	AutoBCS	24.25	29.18	33.26	37.51	38.54
$\sigma_n = 0.05$	D-SPL	9.26	12.71	24.83	30.90	31.66
	MH-SPL	17.89	22.28	28.62	31.60	32.22
	GBsR	18.16	23.46	28.92	33.13	33.79
	AutoBCS	24.24	29.08	32.73	35.25	35.49
$\sigma_n = 0.1$	D-SPL	9.26	12.71	24.26	28.83	29.18
	MH-SPL	17.30	20.96	26.41	29.34	29.64
	GBsR	18.25	21.68	26.66	30.07	30.37
	AutoBCS	24.21	28.77	31.54	31.81	31.59

plots, we can distinctly observe that the reconstructed images seem to be much clearer and contain richer textures with more edges and details. Totally speaking, LSM can indeed facilitate the recovery performance in a large margin, compared with other classic sensing matrices.

B. AutoBCS for noisy reconstruction

This part aims to measure the reconstruction performance of AutoBCS for noisy occasions³. To this end, three conventional BCS methods (D-SPL, MH-SPL, and GBsR) are

³It is worth noting that here we are still using the previously trained network instead of retraining a new AutoBCS under noisy environment.

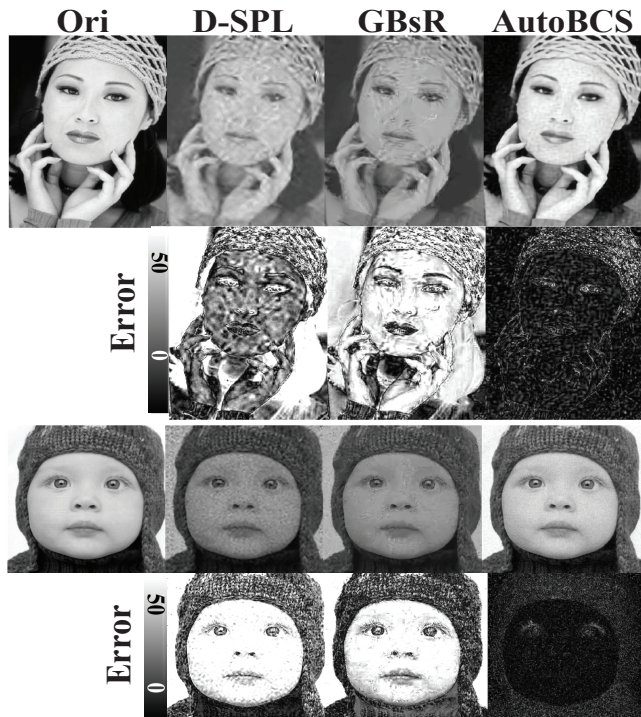


Fig. 11: Comparison of noisy image reconstruction for traditional BCS approaches (D-SPL and GBsR) and AutoBCS on Set5 in case of $\tau = 0.1$ with Gaussian noise of $\sigma_n = 0.1$, where the second and the fourth rows are corresponding image errors. Please zoom in for better comparison.

simultaneously compared with AutoBCS in the setting of dataset Set5 and additive Gaussian noise, where standard derivations of Gaussian noise are $\sigma_n = 0.01$, $\sigma_n = 0.05$, and $\sigma_n = 0.1$, respectively. The average PSNR results at various noise levels are shown in Table V. According to these results, we can clearly see that our proposed AutoBCS consistently outperforms the other competing approaches. For $\sigma_n = 0.01$, our average PSNR gains over D-SPL, MH-SPL, and GBsR methods are larger than 10.05 dB, 5.36 dB and 3.64 dB, respectively. For $\sigma_n = 0.05$, AutoBCS can enhance PSNR on average by approximately 9.49 dB, 4.96 dB and 3.87 dB, respectively. For $\sigma_n = 0.1$, our proposed framework surpasses D-SPL, MH-SPL, and GBsR methods by 8.74 dB, 4.85 dB and 4.18 dB. In particular, we illustrate the visual comparisons at sampling rate $\tau = 0.1$ with Gaussian noise of $\sigma_n = 0.1$ in Fig. 11. From the visual plots, it can be observed that the other BCS algorithms all yield visually annoying artifacts; by contrary, the images recovered by the proposed AutoBCS contain much fewer artifacts and seem to be much smoother.

In summary, the proposed AutoBCS obtains an outstanding performance for noisy reconstruction according to the quantitative and visual results.

VI. CONCLUSION

In this work, we present a novel pure DL-based framework for BCS, called AutoBCS, which replaces the traditional BCS approaches from data acquisition to reconstruction. The

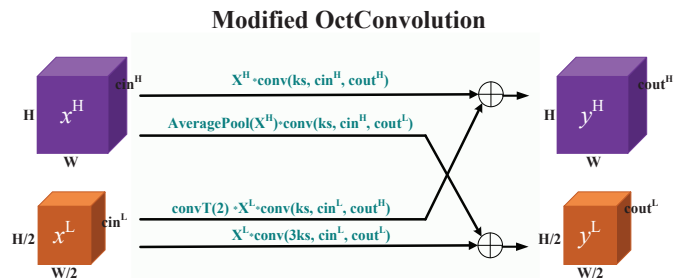


Fig. 12: The concept of modified octave convolution.

proposed AutoBCS develops a learning-based sensing patterns to obtain data acquisition without handcrafting the sparsifying domain and the related parameters, and customizes a subsequent inference model to accomplish fast image reconstruction with low computational cost. In a nutshell, the generated LSM is data-driven and its sampling efficiency is theoretically guaranteed, and the computational complexity of image reconstruction is significantly reduced, through our framework. Our proposed AutoBCS is verified on several image databases, and the corresponding results demonstrate its effectiveness and superiorities, compared with traditional BCS approaches as well as the other newly-developing DL-based methods.

In the future work, we will further investigate why the sampling efficiency of LSM can outperform that of random matrices, although we have shown that LSM meets the theoretical requirements. Moreover, some strong robust modified DL strategies will be considered for noisy image reconstruction occasions. Meanwhile, how to extend our proposed AutoBCS to other image inverse problems, such as inpainting and deconvolution, is another concerned direction of our future work.

APPENDIX A

Part I: Modified octave convolution

Let $\mathbf{X} \in \mathbb{R}^{\{h \times w \times u\}}$ represent the input feature tensor of a convolution layer, where h , w , and u denote the height, width, and channel of the feature maps, respectively. Unlike traditional vanilla convolutions, octave convolution explicitly factorize the feature maps \mathbf{X} along the channel dimension into $\{\mathbf{X}_H, \mathbf{X}_L\}$, where $\mathbf{X}_H \in \mathbb{R}^{\{h \times w \times (1-t)u\}}$ denotes the high resolution features, $\mathbf{X}_L \in \mathbb{R}^{\{h \times w \times tu\}}$ represents the low resolution features, and $t \in [0, 1]$, respectively. Typically, for the input layer of the octave network $t = 0$, and for the following layers $t = 0.5$. In our work, the original octave convolution is specially modified by replacing the nearest interpolation with the transposed convolution. As a consequence, the corresponding outputs of modified octave convolution, $\{\mathbf{Y}_H, \mathbf{Y}_L\}$, can be obtained as following:

$$\begin{aligned} \mathbf{Y}_H &= \text{conv}(\mathbf{X}_H, \mathbf{W}_{H-H}) + \text{convT}(\text{conv}(\mathbf{X}_L, \mathbf{W}_{L-H}), 2), \\ \mathbf{Y}_L &= \text{conv}(\mathbf{X}_L, \mathbf{W}_{L-L}) + \text{conv}(\text{pool}(\mathbf{X}_H, 2), \mathbf{W}_{H-L}), \end{aligned}$$

where $\text{convT}(\cdot, k)$ is the traditional transposed convolution operation with kernels of size $k \times k$, $\text{pool}(\mathbf{X}, k)$ denotes the pooling operation with kernel size $k \times k$, and \mathbf{W} is the learnable

weights of different layers. For visual observation, we illustrate the concept of modified octave convolution in Fig. 12.

Note that the replacement of the nearest interpolation by the transposed convolution will result in that the up-sampling operation becomes a learnable block and can be optimized during the training procedure of our network. Such a modification will degrade more redundancy on the spatial dimension, and obtain better multi-scale representation learning than vanilla convolutions.

Part II: Octave transposed convolution

An octave transposed convolution is designed for our customized octave reconstruction sub-network. Let $\{\mathbf{X}_H, \mathbf{X}_L\}$ be the input feature maps, and $\{\mathbf{Y}_H, \mathbf{Y}_L\}$, $\mathbf{Y}_H \in \mathbb{R}^{\{2h \times 2w \times (1-t)u\}}$, $\mathbf{Y}_L \in \mathbb{R}^{\{2h \times 2w \times tu\}}$, represent the output features. Then we can formulate the octave transposed convolution as:

$$\begin{aligned} \mathbf{Y}_H &= \text{convT}(\mathbf{X}_H, \mathbf{W}_{H-H}, 2) + \text{convT}(\mathbf{X}_L, 4), \\ \mathbf{Y}_L &= \text{convT}(\mathbf{X}_L, 2) + \text{conv}(\mathbf{X}_H, \mathbf{W}_{H-L}). \end{aligned}$$

Such an octave transposed convolution will allow the feature maps $\{\mathbf{X}_H, \mathbf{X}_L\}$ double their spatial resolution, and can help build the expanding part of the octave reconstruction sub-network.

APPENDIX B

To begin with, we show the research of RIP-based guarantee for LSM \mathbf{P}_A , following the works of [8, 22].

Theorem 1. *An $m_a \times A^2$ LSM, trained from AutoBCS network, satisfies the (s_a, δ_a) -RIP with the prescribed δ_a and any $s_a \leq c_0 A^2 / \log(m_a/s_a)$ with probability exceeding $1 - 2e^{-c_1 m_a}$, where two constants $c_0, c_1 \geq 0$ and s_a is sparsity of an arbitrary signal $\in \mathbb{R}^{A^2}$.*

Theorem 1 implies that LSM meets asymptotically optimal sampling performance. Moreover, this property straightforward allows us to pose other guarantees for LSM via the Gershgorin circle theorem, such as the coherence and spark property. For example, the coherence property can be bridged to the (s_a, δ_a) -RIP. Therefore, it can be directly posed the following condition on our trained LSM that guarantees sampling efficiency.

Theorem 2. *For an $m_a \times A^2$ LSM satisfying the (s_a, δ_a) -RIP, then the coherence $\mu(\mathbf{P}_A)$ and spark of LSM follow $\mu(\mathbf{P}_A) = \delta_a / (s_a - 1)$ and $\text{spark}(\mathbf{P}_A) > 2s_a$, respectively.*

Very similar results of sampling efficiency hold for random matrices, such as Gaussian and Bernoulli matrices. For each s_a -sparse signal to be uniquely representation by its samples \mathbf{y}_s , we can show that \mathbf{P}_A meets the $(2s_a, \delta_a)$ -RIP with $\delta_a > 0$, as it indicates that all sets of $2s_a$ columns of \mathbf{P}_A are linearly independent, that is, $\text{spark}(\mathbf{P}_A) > 2s_a$. From a theoretical aspect, the RIP of LSM enables recovery guarantees that are more robust than those based on coherence and spark properties. In addition, we can also draw similar conclusions by analyzing the elements' characteristics of \mathbf{P}_A .

REFERENCES

- [1] E. J. Candès, J. Romberg, and T. Tao, "Robust uncertainty principles: Exact signal reconstruction from highly incomplete frequency information," *IEEE Transactions on Information Theory*, vol. 52, no. 2, pp. 489–509, 2006.
- [2] D. L. Donoho, "Compressed sensing," *IEEE Transactions on Information Theory*, vol. 52, no. 4, pp. 1289–1306, 2006.
- [3] M. F. Duarte, M. A. Davenport, D. Takhar, J. N. Laska, T. Sun, K. F. Kelly, and R. G. Baraniuk, "Single-pixel imaging via compressive sampling," *IEEE Signal Processing Magazine*, vol. 25, no. 2, pp. 83–91, 2008.
- [4] L. Y. Zhang, K. Wong, Y. Zhang, and J. Zhou, "Bi-level protected compressive sampling," *IEEE Transactions on Multimedia*, vol. 18, no. 9, pp. 1720–1732, 2016.
- [5] Y. Zhang, Y. Xiang, L. Y. Zhang, Y. Rong, and S. Guo, "Secure wireless communications based on compressive sensing: A survey," *IEEE Communications Surveys and Tutorials*, vol. 21, no. 2, pp. 1093–1111, 2019.
- [6] G. Mei, X. Wu, Y. Wang, M. Hu, J.-A. Lu, and G. Chen, "Compressive-sensing-based structure identification for multilayer networks," *IEEE Transactions on Cybernetics*, vol. 48, no. 2, pp. 754–764, 2017.
- [7] S. Zhang, X. Li, Q. Lin, and K. Wong, "Nature-inspired compressed sensing for transcriptomic profiling from random composite measurements," *IEEE Transactions on Cybernetics*, pp. 1–12, 2019.
- [8] Y. C. Eldar and G. Kutyniok, *Compressed sensing: Theory and applications*. Cambridge University Press, 2012.
- [9] N. Ahmed, T. Natarajan, and K. R. Rao, "Discrete cosine transform," *IEEE Transactions on Computers*, vol. 100, no. 1, pp. 90–93, 1974.
- [10] L. He and L. Carin, "Exploiting structure in wavelet-based Bayesian compressive sensing," *IEEE Transactions on Signal Processing*, vol. 57, no. 9, pp. 3488–3497, 2009.
- [11] M. Usman, C. Prieto, T. Schaeffter, and P. Batchelor, "K-t group sparse: A method for accelerating dynamic MRI," *Magnetic Resonance in Medicine*, vol. 66, no. 4, pp. 1163–1176, 2011.
- [12] Z. Lai, X. Qu, Y. Liu, D. Guo, J. Ye, Z. Zhan, and Z. Chen, "Image reconstruction of compressed sensing MRI using graph-based redundant wavelet transform," *Medical Image Analysis*, vol. 27, pp. 93–104, 2016.
- [13] R. G. Baraniuk, V. Cevher, M. F. Duarte, and C. Hegde, "Model-based compressive sensing," *IEEE Transactions on Information Theory*, vol. 56, no. 4, pp. 1982–2001, 2010.
- [14] S. Ravishankar, B. E. Moore, R. R. Nadakuditi, and J. A. Fessler, "Low-rank and adaptive sparse signal (LASSI) models for highly accelerated dynamic imaging," *IEEE Transactions on Medical Imaging*, vol. 36, no. 5, pp. 1116–1128, 2017.
- [15] W. Dong, G. Shi, X. Li, Y. Ma, and F. Huang, "Compressive sensing via nonlocal low-rank regularization," *IEEE Transactions on Image Processing*, vol. 23, no. 8,

- pp. 3618–3632, 2014.
- [16] E. J. Candès, “The restricted isometry property and its implications for compressed sensing,” *Comptes Rendus Mathématique*, vol. 346, no. 9-10, pp. 589–592, 2008.
- [17] M. Elad, *Sparse and redundant representations: From theory to applications in signal and image processing*. Springer Science & Business Media, 2010.
- [18] A. Cohen, W. Dahmen, and R. DeVore, “Compressed sensing and best k -term approximation,” *Journal of the American Mathematical Society*, vol. 22, no. 1, pp. 211–231, 2009.
- [19] S. Li and G. Ge, “Deterministic construction of sparse sensing matrices via finite geometry,” *IEEE Transactions on Signal Processing*, vol. 62, no. 11, pp. 2850–2859, 2014.
- [20] H. Gan, S. Xiao, Y. Zhao, and X. Xue, “Construction of efficient and structural chaotic sensing matrix for compressive sensing,” *Signal Processing: Image Communication*, vol. 68, pp. 129–137, 2018.
- [21] H. Gan, S. Xiao, and F. Liu, “Chaotic binary sensing matrices,” *International Journal of Bifurcation and Chaos*, vol. 29, no. 09, p. 1950121, 2019.
- [22] R. Baraniuk, M. Davenport, R. DeVore, and M. Wakin, “A simple proof of the restricted isometry property for random matrices,” *Constructive Approximation*, vol. 28, no. 3, pp. 253–263, 2008.
- [23] A. Maleki and D. L. Donoho, “Optimally tuned iterative reconstruction algorithms for compressed sensing,” *IEEE Journal of Selected Topics in Signal Processing*, vol. 4, no. 2, pp. 330–341, 2010.
- [24] J. Yang and Y. Zhang, “Alternating direction algorithms for ℓ_1 -problems in compressive sensing,” *SIAM Journal on Scientific Computing*, vol. 33, no. 1, pp. 250–278, 2011.
- [25] D. L. Donoho, A. Maleki, and A. Montanari, “Message-passing algorithms for compressed sensing,” *Proceedings of the National Academy of Sciences*, vol. 106, no. 45, pp. 18914–18919, 2009.
- [26] L. Gan, “Block compressed sensing of natural images,” in *2007 15th International conference on digital signal processing*, pp. 403–406, IEEE, 2007.
- [27] B. Adcock and A. C. Hansen, “Generalized sampling and infinite-dimensional compressed sensing,” *Foundations of Computational Mathematics*, vol. 16, no. 5, pp. 1263–1323, 2016.
- [28] Z. Yang, L. Xie, and C. Zhang, “Variational Bayesian algorithm for quantized compressed sensing,” *IEEE Transactions on Signal Processing*, vol. 61, pp. 2815–2824, June 2013.
- [29] V. Cevher, P. Indyk, C. Hegde, and R. G. Baraniuk, “Recovery of clustered sparse signals from compressive measurements,” tech. rep., Rice Univ Houston Tx Dept of Electrical and Computer Engineering, 2009.
- [30] Y. L. Polo, Y. Wang, A. Pandharipande, and G. Leus, “Compressive wide-band spectrum sensing,” in *2009 IEEE International Conference on Acoustics, Speech and Signal Processing*, pp. 2337–2340, IEEE, 2009.
- [31] S. Ji, D. Dunson, and L. Carin, “Multitask compressive sensing,” *IEEE Transactions on Signal Processing*, vol. 57, no. 1, pp. 92–106, 2008.
- [32] S. Mun and J. E. Fowler, “Block compressed sensing of images using directional transforms,” in *2009 16th IEEE International Conference on Image Processing*, pp. 3021–3024, IEEE, 2009.
- [33] J. E. Fowler, S. Mun, and E. W. Tramel, “Multi-scale block compressed sensing with smoothed projected landweber reconstruction,” in *2011 19th European Signal Processing Conference*, pp. 564–568, IEEE, 2011.
- [34] J. Zhang, D. Zhao, C. Zhao, R. Xiong, S. Ma, and W. Gao, “Image compressive sensing recovery via collaborative sparsity,” *IEEE Journal on Emerging and Selected Topics in Circuits and Systems*, vol. 2, no. 3, pp. 380–391, 2012.
- [35] J. Zhang, D. Zhao, and W. Gao, “Group-based sparse representation for image restoration,” *IEEE Transactions on Image Processing*, vol. 23, no. 8, pp. 3336–3351, 2014.
- [36] C. Chen, E. W. Tramel, and J. E. Fowler, “Compressed-sensing recovery of images and video using multihypothesis predictions,” in *2011 Conference Record of the Forty Fifth Asilomar Conference on Signals, Systems and Computers*, pp. 1193–1198, IEEE, 2011.
- [37] Y. Yang, J. Sun, H. Li, and Z. Xu, “ADMM-CSNet: A deep learning approach for image compressive sensing,” *IEEE Transactions on Pattern Analysis and Machine Intelligence*, vol. 42, no. 3, pp. 521–538, 2020.
- [38] J. Zhang and B. Ghanem, “ISTA-Net: Interpretable optimization-inspired deep network for image compressive sensing,” in *Proceedings of the IEEE Conference on Computer Vision and Pattern Recognition*, pp. 1828–1837, 2018.
- [39] K. Kulkarni, S. Lohit, P. Turaga, R. Kerviche, and A. Ashok, “ReconNet: Non-iterative reconstruction of images from compressively sensed measurements,” in *Proceedings of the IEEE Conference on Computer Vision and Pattern Recognition*, pp. 449–458, 2016.
- [40] H. Yao, F. Dai, S. Zhang, Y. Zhang, Q. Tian, and C. Xu, “DR²-net: Deep residual reconstruction network for image compressive sensing,” *Neurocomputing*, vol. 359, pp. 483–493, 2019.
- [41] A. Adler, D. Boubilil, and M. Zibulevsky, “Block-based compressed sensing of images via deep learning,” in *2017 IEEE 19th International Workshop on Multimedia Signal Processing*, pp. 1–6, 2017.
- [42] W. Shi, F. Jiang, S. Zhang, and D. Zhao, “Deep networks for compressed image sensing,” in *2017 IEEE International Conference on Multimedia and Expo*, pp. 877–882, 2017.
- [43] W. Shi, F. Jiang, S. Liu, and D. Zhao, “Image compressed sensing using convolutional neural network,” *IEEE Transactions on Image Processing*, vol. 29, pp. 375–388, 2019.
- [44] J. E. Fowler, S. Mun, E. W. Tramel, *et al.*, “Block-based compressed sensing of images and video,” *Foundations and Trends in Signal Processing*, vol. 4, no. 4, pp. 297–416, 2012.

- [45] A. Mousavi, A. B. Patel, and R. G. Baraniuk, "A deep learning approach to structured signal recovery," in *2015 53rd Annual Allerton Conference on Communication, Control, and Computing*, pp. 1336–1343, IEEE, 2015.
- [46] Y. Chen, H. Fan, B. Xu, Z. Yan, Y. Kalantidis, M. Rohrbach, S. Yan, and J. Feng, "Drop an octave: Reducing spatial redundancy in convolutional neural networks with octave convolution," in *Proceedings of the IEEE International Conference on Computer Vision*, pp. 3435–3444, 2019.
- [47] S. Gao, M. Cheng, K. Zhao, X. Zhang, M. Yang, and P. H. S. Torr, "Res2Net: A new multi-scale backbone architecture," *IEEE Transactions on Pattern Analysis and Machine Intelligence*, pp. 1–10, 2019.
- [48] R. Durall, F. Pfrendt, and J. Keuper, "Stabilizing GANs with octave convolutions," *CoRR*, vol. abs/1905.12534, 2019.
- [49] A. Eftekhari, H. L. Yap, C. J. Rozell, and M. B. Wakin, "The restricted isometry property for random block diagonal matrices," *Applied and Computational Harmonic Analysis*, vol. 38, no. 1, pp. 1–31, 2015.
- [50] N. Koep, A. Behboodi, and R. Mathar, "The restricted isometry property of block diagonal matrices for group-sparse signal recovery," *arXiv preprint arXiv:1901.06214*, 2019.
- [51] O. Ronneberger, P. Fischer, and T. Brox, "U-net: Convolutional networks for biomedical image segmentation," in *International Conference on Medical image computing and computer-assisted intervention*, pp. 234–241, Springer, 2015.
- [52] C. Li, W. Yin, and Y. Zhang, "User's guide for TVAL3: TV minimization by augmented lagrangian and alternating direction algorithms," *CAAM Report*, vol. 20, no. 46-47, p. 4, 2009.
- [53] A. Hore and D. Ziou, "Image quality metrics: PSNR vs. SSIM," in *2010 20th International Conference on Pattern Recognition*, pp. 2366–2369, IEEE, 2010.
- [54] P. Arbelaez, M. Maire, C. Fowlkes, and J. Malik, "Contour detection and hierarchical image segmentation," *IEEE Transactions on Pattern Analysis and Machine Intelligence*, vol. 33, no. 5, pp. 898–916, 2011.
- [55] J. Kim, J. Kwon Lee, and K. Mu Lee, "Accurate image super-resolution using very deep convolutional networks," in *Proceedings of the IEEE Conference on Computer Vision and Pattern Recognition*, pp. 1646–1654, 2016.
- [56] M. Bevilacqua, A. Roumy, C. Guillemot, and M. L. Alberi-Morel, "Low-complexity single-image super-resolution based on nonnegative neighbor embedding," in *Proceeding of British Machine Vision Conference*, pp. 135.1–135.10, BMVA Press, 2012.
- [57] R. Zeyde, M. Elad, and M. Protter, "On single image scale-up using sparse-representations," in *International Conference on Curves and Surfaces*, pp. 711–730, Springer, 2010.
- [58] D. Martin and C. Fowlkes, "A database of human segmented natural images and its application to evaluating segmentation algorithms and measuring ecological statis-
- tics," in *Proceedings of 8th International Conference on Computer Vision*, vol. 2, pp. 416–423, 2001.